

Local Strain and Polarization Mapping in Ferrielectric Materials

Sabine M. Neumayer, John A. Brehm, Lei Tao, Andrew O'Hara, Panchapakesan Ganesh, Stephen Jesse, Michael A. Susner, Michael A. McGuire, Sokrates T. Pantelides, Petro Maksymovych, and Nina Balke*



Cite This: *ACS Appl. Mater. Interfaces* 2020, 12, 38546–38553



Read Online

ACCESS |



Metrics & More



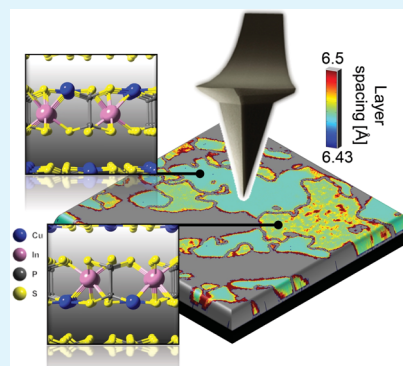
Article Recommendations



Supporting Information

ABSTRACT: CuInP_2S_6 (CIPS) is a van der Waals material that has attracted attention because of its unusual properties. Recently, a combination of density functional theory (DFT) calculations and piezoresponse force microscopy (PFM) showed that CIPS is a uniaxial quadruple-well ferrielectric featuring two polar phases and a total of four polarization states that can be controlled by external strain. Here, we combine DFT and PFM to investigate the stress-dependent piezoelectric properties of CIPS, which have so far remained unexplored. The two different polarization phases are predicted to differ in their mechanical properties and the stress sensitivity of their piezoelectric constants. This knowledge is applied to the interpretation of ferroelectric domain images, which enables investigation of local strain and stress distributions. The interplay of theory and experiment produces polarization maps and layer spacings which we compare to macroscopic X-ray measurements. We found that the sample contains only the low-polarization phase and that domains of one polarization orientation are strained, whereas domains of the opposite polarization direction are fully relaxed. The described nanoscale imaging methodology is applicable to any material for which the relationship between electromechanical and mechanical characteristics is known, providing insight on structural, mechanical, and electromechanical properties down to ~ 10 nm length scales.

KEYWORDS: piezoresponse force microscopy, piezoelectric constant, van der Waals materials, stress mapping, copper indium thiophosphate



1. INTRODUCTION

The family of metal thiophosphates is characterized by a $[\text{P}_2\text{S}_6]^{4-}$ framework stabilized by metal cations.¹ The van der Waals (vdW) layered structure of these materials allows easy exfoliation of ultrathin flakes that exhibit a wide range of intriguing electromechanical, optical, electronic, and magnetic properties. Moreover, the absence of dangling bonds in metal-thiophosphate surfaces enables the construction of ideal interfaces to fabricate heterostructures with two-dimensional materials such as graphene and MoS_2 .² A particularly interesting metal-thiophosphate compound is CuInP_2S_6 (CIPS), which has a non-centrosymmetric monoclinic structure in its ferrielectric state (space group Cc). The interest in CIPS arises from its large and negative out-of-plane electrostrictive coefficient $Q_{33} = -3.2 \text{ m}^4/\text{C}^2$, a value that allows for a strong piezoelectric response despite relatively low polarization values.³ Experimentally reported polarization values range between 2.6 and $5 \mu\text{C}/\text{cm}^2$, obtained in nonlocal switching experiments where current peaks measured on electrodes during voltage sweeps indicate the switched polarization. Moreover, polarization switching has been observed in ultrathin samples^{4,5} and remarkable electrocaloric performance has been detected.⁶ In addition, high ionic conductivity combined with lattice resilience to defects enables reversible extraction of Cu from this remarkable material.⁷

Recently, we reported density functional theory (DFT) calculations that predicted a uniaxial quadruple-well potential in ferrielectric CIPS.⁸ As a result, CIPS features two stable ferrielectric phases with strongly overlapping energy landscapes and a total of four polarization states, in which the Cu atoms are either located within the $[\text{P}_2\text{S}_6]^{4-}$ lamellae or are displaced into the vdW gaps (Figure 1a). The first phase with stable Cu positions within the layers has a polarization value $P_3 \sim 5 \mu\text{C}/\text{cm}^2$ and a c -lattice parameter of 13.09 Å, whereas the second phase with stable Cu positions in the vdW gap has a polarization value $P_3 \sim 11 \mu\text{C}/\text{cm}^2$ and a c lattice parameter of 12.87 Å as determined by DFT.⁸ The two phases, therefore, have been designated as low-polarization (LP) and high-polarization (HP) phases. DFT calculations of polarization and stress as function of c lattice parameter were used to predict the piezoelectric constant d_{33} for each of the two phases around their equilibrium zero-stress condition, finding $-15.6 \text{ pm}/\text{V}$

Received: May 20, 2020

Accepted: July 29, 2020

Published: July 29, 2020



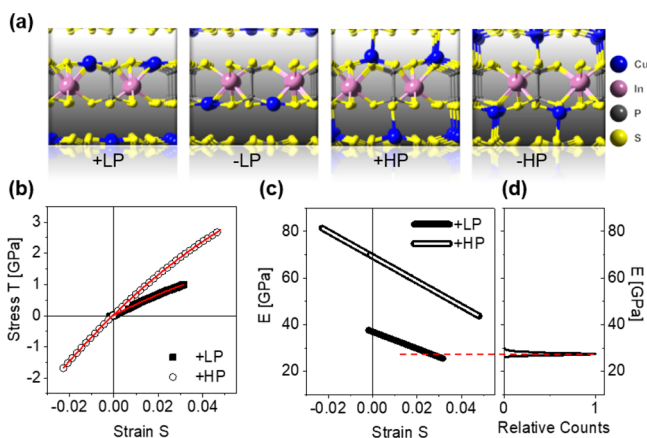


Figure 1. (a) Structure of all four polarization states in CIPS. (b) Calculated stress–strain curves for the +LP and +HP polarization state. Red lines indicate quadratic fit functions. (c) Derivative of the fitted stress–strain curves to obtain elastic-modulus values. (d). Histogram of locally measured elastic modulus in a $3 \times 3 \mu\text{m}^2$ area. The red line is a guide to the eye to compare (c,d).

for the LP phase and 2.5 pm/V for the HP phase. These values have been confirmed experimentally using local mapping and bias-dependent quantification of the piezoelectric constants by piezoresponse force microscopy (PFM) measurements.⁸ At the same time, it was shown that the quadruple well is highly sensitive to strain and that local strains are responsible for LP or HP phase stabilization. Therefore, CIPS shows great promise for the tuning of the functional properties of CIPS by strain, provided the strain can be experimentally verified and subsequently controlled. This result also introduces an opportunity to image local strains, stresses, and polarizations through measurement of the changes in the piezoelectric constant these variables introduce, as long as the relative dependences are known. This technique would enable imaging of these properties in a non-destructive way on length scales from 10s of nm to 10 of mm which would be complimentary to macroscopic strain and polarization mapping in ferroelectrics using X-ray^{9–12} and I – V curves on capacitor structures,^{6,13–15} as well as atomic scale approaches using scanning transmission electron microscopy.^{16–21}

Here, we report the imaging of the mechanical properties of the two polarization phases in CIPS as well as local polarization, stress, and strain distribution by scanning probe microscopy (SPM) on length scales of ~ 10 s of nm. The extraction of rich information from a single SPM image is enabled by theoretically predicted relationships between stress,

strain, and polarization for the LP and HP phases in CIPS using DFT. The theoretical methodology is described in⁸ and was extended to cover a very large range of c lattice parameters to span a large stress and strain range. The results are predictions of the strain-dependent elastic modulus as well as the stress-dependent piezoelectric constant d_{33} . While Young's modulus is directly experimentally verified using contact-resonance atomic force microscopy (AFM) approaches, the piezoelectric constant is measured by PFM, which is a commonly used SPM technique based on measuring the electromechanical sample response to an AC voltage applied to the cantilever tip by detecting its dynamic deflection.^{22–25} Furthermore, local strain maps are used to extract maps of layer spacing which are then directly compared to published X-ray data, resulting in good agreement and showing that some strain relaxation occurs at the CIPS surface. The overall procedure outlines a pathway to understanding material functionality at a new level and allows us to gain insights and subsequently tune material properties at length scales not accessible otherwise.

2. RESULTS AND DISCUSSION

The two polar phases of CIPS, LP and HP, result in four distinct polarization states shown in Figure 1a. The LP states have stable Cu positions in the layer, whereas the HP states have stable Cu positions within the vdW gap. DFT calculations provided the polarization for each polarization state and also described how these polarization values change as function of stress T and strain S .⁸ Because of the uniaxial nature of CIPS as a vdW material, we only considered the z -direction components of the polarization, strain, and stress (P_z , S_{33} , T_{33}) which we shall refer to without their indices, that is, as P , S , and T . We only show results for the two positive polarization states of the LP and HP phases because of symmetry considerations. We do not consider in-plane components of polarization, strain, and stress because the polarization components along x and y are negligible,⁸ and the material has a near-zero Poisson's ratio,²⁶ which means out-of-plane and in-plane strains and stresses do not influence each other.

First, we explore the mechanical properties, that is, the strain S versus stress T curves for each individual phase as obtained from theory. In Figure 1b, it can be clearly seen that the two phases show different slopes in the stress–strain curves. For the +LP state, small discontinuities in the stress–strain curve were present. They can be explained by in-plane Cu motion and have been corrected (Figure S1). The stress–strain curves show a viscoelastic behavior that is best fitted using parabolic curves. As a consequence, the elastic modulus E changes

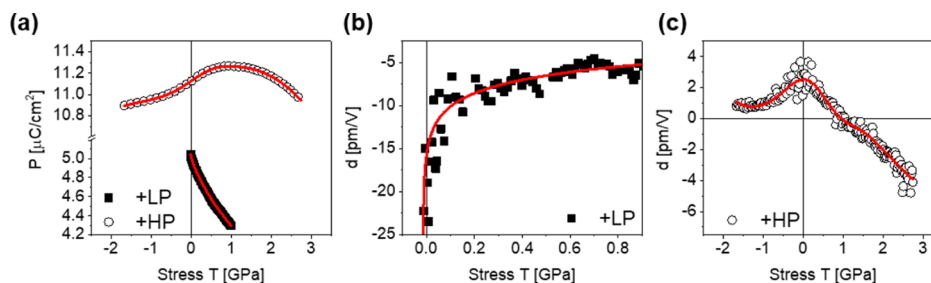


Figure 2. (a) Theoretical polarization as a function of stress for the +LP and +HP polarization states. Red lines indicate empirical fitting functions. Numerical derivative of theoretical polarization–stress points to obtain values for the piezoelectric constant d for the (b) +LP state and (c) +HP state. Red curves indicate the derivative of the fit functions in (a).

linearly as a function of strain according to $E = \partial T/\partial S$. It was found that the HP phase has an elastic modulus almost twice as high as that of the LP phase (Figure 1c).

We employed contact-resonance AFM to test the theoretical predictions against experimental measurements. Here, the cantilever is mechanically excited using a photothermal method.²⁷ To quantify the elastic modulus of CIPS, we extracted the mechanical properties of the material by analyzing the tip–sample contact interactions with mathematical models^{28–30} and in turn compared these results with the HOPG elastic modulus ($E = 18$ GPa). We performed these measurements across a $3 \times 3 \mu\text{m}^2$ sample area, and the histogram of the measured values is shown in Figure 1d. The average measured elastic modulus is 27 GPa which matches the predicted value for a strain of 0.03 for the LP phase. A strained polarization phase is expected because local strain was proposed as the mechanism that stabilizes the LP or HP phase by eliminating the small energy barrier between them.⁸

The theoretical calculations also reveal a nonlinear relation between polarization and stress (Figure 2a). The +LP state has a smaller polarization which decreases with increasing positive stress. Under negative stress (compression), the LP phase is not stable. In contrast, the +HP state is stable over a wide positive and negative stress range and shows a dependency that is both non-monotonic and nonlinear. The theoretical data points were fitted using empirical functions; we plot the derivatives of these functions together with the numerical derivatives of the theoretical data in Figure 2b for the +LP state and in Figure 2c for the +HP state. The derivative of $P(T)$ is equivalent to the piezoelectric constant d according to the relationship $d = \partial P/\partial T$. The good match between the calculated values and the values obtained from the empirical fit of the calculated values supports the accuracy of the chosen fit functions and reveals the presence of a highly strain-dependent piezoelectric constant. For the +LP state, the piezoelectric constant is negative and decreases in amplitude under positive stress (Figure 2b). In contrast, the +HP state has a smaller (and positive) piezoelectric constant which decreases from its unstressed value if either positive or negative stress is applied. If the positive stress is high enough (>1 GPa), the piezoelectric constant of the +HP state becomes negative (Figure 2c). We fit the theoretical data with empirical functions so that we can match the theoretical curves to measured values of the piezoelectric constant and derive values for the stress, strain, and polarization.

We used spatially resolved PFM to measure the piezoelectric constant. Steps toward quantification of d from PFM have been reported using different approaches, including low-frequency measurements far away from contact resonance frequencies and the use of static sensitivity or background removal,³¹ calibration on domain walls,^{32,33} specialized cantilevers,^{34,35} and interferometric approaches that complement PFM measurements on top electrodes.^{36–38} Other recent work includes the modeling of the cantilever beam shape and the introduction of a correction factor to compare cantilevers of different stiffnesses for PFM performed near or at the contact resonance frequency.^{39,40} It is not only important to quantify the surface displacement but also to consider the non-piezoelectric PFM contrast mechanism⁴¹ including cross-talk,^{42,43} electrostatic forces between cantilever and sample,⁴⁴ Joule heating,^{45,46} charge injection,⁴⁷ and ionic motion.⁴⁸

We performed PFM on a phase-separated sample containing CIPS and the non-ferrielectric $\text{In}_{4/3}\text{P}_2\text{S}_6$ (IPS) phase (Figure

3a). Separating the response from the CIPS and IPS areas (Figure S2a,b) allowed us to use IPS as an internal reference to

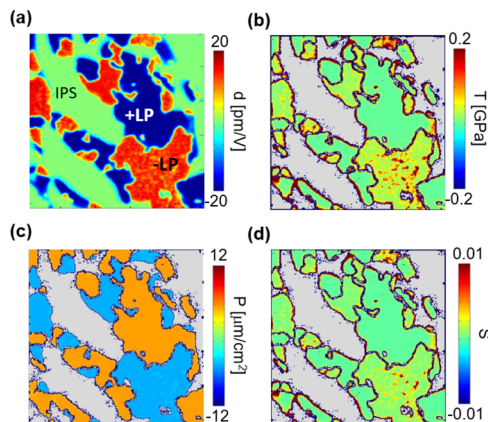


Figure 3. (a) Map of piezoelectric constant obtained by PFM in a $3 \times 3 \mu\text{m}^2$ area. After comparison to theoretical curves, maps of (b) stress, (c) polarization, and (d) strain can be derived.

estimate non-ferrielectric signal contributions such as electrostatics. This procedure is warranted by the fact that the two phases are not distinguishable in Kelvin probe force microscopy after PFM imaging and that the non-hysteretic bias-dependent contributions to measured PFM hysteresis loops are identical for CIPS and IPS.³ We quantified the PFM signal (pm/V) using cantilever contact dynamics as described elsewhere.³⁹ The values of d for +LP and –LP domains are asymmetric and deviate from the theoretical prediction at zero stress (Figure S2c).

Once the measured piezoelectric constant values were quantified, each CIPS pixel in a $3 \times 3 \mu\text{m}^2$ area was compared to the theoretical curves of $d(T)$. The corresponding value of T was then used to calculate the polarization from the $P(T)$ dependency and in turn compared to the theoretical $S(T)$ curves to extract S (Figure S3). We calculated the lattice constant and layer spacing from S using the knowledge of the equilibrium lattice constants of the individual polar phases and crystal symmetry of the LP and HP phases. Based on the comparison between experimental and theoretical d values, we found only unique solutions, that is, each d value can be assigned unambiguously to one of the four polarization states (Figure S4). We were able to assign the +LP and –LP polarization states to the PFM image in Figure 3a. Depending on the d value, the comparison between experimental and theoretical values can yield more than one solution. In those cases, extra conditions need to be applied, such as minimization of overall stress or strain, elastically stored energy, or c -lattice parameter variation. These options are not discussed further here.

As a result of combining experiment and theory, we derived local maps of stress, polarization, and strain with the help of the empirical fit functions (Figure 3b–d). The polarization shows positive and negative values corresponding to the +LP and –LP polarization states at around $\pm 5 \mu\text{C}/\text{cm}^2$ based on the DFT calculations. This corresponds well with a measured polarization of $\pm 4.3 \mu\text{C}/\text{cm}^2$ on a stoichiometric CIPS sample with macroscopic electrodes (Figure S5a,b). One observation is that the strain and stress maps show different contrasts for the two kinds of domains. The +LP domains evince stress/strain values that are both low in magnitude and uniform in

their distribution, whereas the $-LP$ domains show larger values for stress/strain together with a non-uniform texture. The corresponding histograms are shown in Figure S5c,d, respectively. This level of insight about local material properties based on the comparison between experiment and theory is very powerful because properties of polarization, strain, and stress cannot be easily measured on such small length scales. For example, polarization is normally obtained by collecting current as a function of voltage measured on micrometer-sized capacitors.

In order to verify the validity of the proposed method, we extracted a map of the layer spacing d_L by first constructing a c -lattice parameter map from the strain map using the theoretically calculated equilibrium c -lattice parameter of 13.09 Å for the LP phase. The layer spacing is defined as the distance between the midplane of two adjacent layers, equivalent to the sum of the thickness of one layer and one vdW gap. The layer spacing d_L is calculated according to $d_L = 0.5 \cdot c \cdot \sin(\beta)$ with β being the monoclinic angle, which is assumed to be strain and stress independent. Here, we used $\beta = 99.1^\circ$ as the theoretically calculated value, which is in good agreement with experimental data published by Maisonneuve et al. (note that they use a non-standard but equivalent setting for the monoclinic unit cell).⁵⁰ The corresponding layer spacing for the theoretically calculated equilibrium c -lattice parameter of 13.09 Å for the LP phase is 6.4626 Å. The layer spacing map (Figure 4a) shows a bimodal distribution

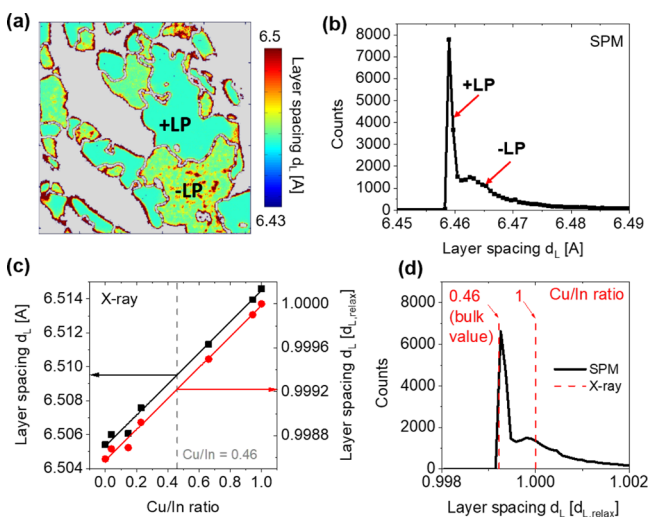


Figure 4. (a) Map of local layer spacing of the layered CIPS sample extracted from SPM strain maps and the equilibrium c -lattice parameter of 13.09 Å in a $3 \times 3 \mu\text{m}^2$ area and (b) corresponding histogram. (c) Layer spacing extracted from X-ray data as a function of Cu/In ratio in absolute and relative units as published by Susner et al.⁴⁹ (d) Histogram of measured layer spacing by SPM in relative units in comparison to X-ray values measured for a Cu/In ratios of 1 and 0.46. The relative layer spacing refers to the unstrained fully stoichiometric CIPS phase with a layer spacing of $d_{L,relax}$.

representing the +LP and $-LP$ domains (Figure 4b). The +LP polarization state has a layer spacing of about 6.459 Å and is represented by a sharp, narrow peak, further showing the uniform strain state of this state. In contrast, the $-LP$ polarization state has a distribution around 6.463 Å that is (1) quite wide and (2) skewed toward larger layer spacings.

The layer spacing map can be directly compared to information obtained on the macroscopic scale from X-ray data. As published by Susner et al.,⁴⁹ the layer spacing of a CIPS/IPS composite sample depends strongly on the Cu/In ratio, which results in different strain and has been reported to range between 6.5054 Å (for IPS) and 6.5146 Å (for fully stoichiometric CIPS). Here, the layer spacing of CIPS along the c -axis is strained due to the smaller layer spacing of the IPS phase along the a -axis. The layer spacing d_L shows a nearly linear trend with Cu/In ratio (Figure 4c). It can be seen that the experimental values are larger than shown in Figure 4a. This is due to the fact that theoretically predicted c lattice parameter of 13.09 Å is smaller than the experimentally determined value of 13.187 Å (standardized crystallographic data).⁵⁰ Therefore, for comparison of combined SPM/theory and X-ray data, we normalized the layer spacings by the respective equilibrium layer spacing from experiment and theory. More specifically, this is the layer spacing for the unstrained case $d_{L,relax}$ that is, Cu/In = 1 from experiment and $T = 0$ GPa from theory (Figure 4d). The theoretical and experimental values used for the normalization are therefore 6.4626 and 6.5146 Å, respectively. Based on Figure 4a, we can estimate the composition of the CIPS and IPS phases to be 53.6 and 46.4%, respectively. Taking the chemical composition of CIPS and IPS into account, we can estimate a Cu/In ratio of 0.46 for the area shown in Figure 4a, which is higher than the nominal ratio of 0.33. From Figure 4c, we can estimate a normalized layer spacing from the X-ray data for the ratio of 0.46 to be 0.9992, which matches the layer spacing distribution of the +LP domain as shown in Figure 4d. Therefore, we can conclude that the +LP domain with uniform stress distribution matches the expected layer spacing from bulk X-ray measurements, which further confirms the validity of our theoretical description and experimental approach. The c lattice parameter of the $-LP$ domains are larger and match the bulk value from X-ray for a Cu/In ratio of 1. This suggests that this particular polarization orientation is relaxed and less strained by the presence of the IPS. As there is little evidence of a bimodal distribution of layer spacing in the X-ray data, we propose that the relaxed domains only exist at the sample surface.

The asymmetry in strain relaxation at the surface can be further explained by performing structural DFT relaxations on an 8-layer CIPS stack with uniform polarization direction so that the top surface represents a $-LP$ domain, while the bottom surface represents a +LP domain (Figure 5a). We find that both CIPS surfaces induce expansion of the layer spacing as defined by the In–In distance, but the strain relaxation is asymmetric (Figure 5b). The $-LP$ surface has a stronger driving force to expand which is consistent with our observation of a relaxed $-LP$ domain. One reason for this asymmetry is the inherent difference in the Cu atom positions relative to the two surfaces and the strongly asymmetric relaxation of the surface-layer Cu atoms, which undergo a large shift toward the center of the layer on the bottom surface (Figure 5c). Note that the theoretical calculation is simulating an unstrained CIPS phase, whereas the experimental data was obtained on a strained sample with different bulk layer spacing. Therefore, when comparing Figures 4d and 5b, the bulk layer spacing is the reference point. In that case, both experiment and theory show that the $-LP$ domain relaxes above its bulk value which is for a Cu/In ratio of 0.46 in the experimental data.

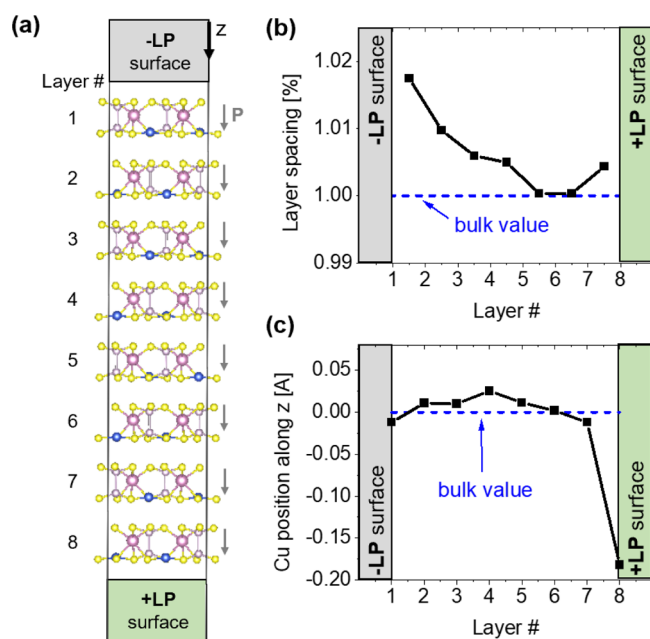


Figure 5. (a) Structural relaxation of an 8-layer thick unstrained CIPS stack with uniform polarization pointing downward modeled with DFT. The top surface represent a $-LP$ domain, whereas the bottom surface represents a $+LP$ domain. (b) Layer spacing and (c) Cu position after relaxation in comparison to bulk values.

We note that local changes in piezoelectric constant measured by PFM and derivation from theoretically predicted values can also be due to non-strain-related phenomena such as (i) tip wear, (ii) locally varying mechanical clamping under the SPM tip, (iii) differently oriented domains in the probed volume, (iv) changes in cantilever mode shapes based on variations of local tip-sample contact stiffness, and (v) the presence of unwanted signal contributions such as electrostatics and local variations thereof. We expect that (i–iii) would affect $+LP$ and $-LP$ domains the same way and (iv) as well as (v) were tested for according to published procedures.^{44,51,52} Moreover, for more complex materials, the effectively measured piezoelectric coefficient could contain contributions from other tensor elements.^{53–55} In this case, precise sample alignment is important and the measured response may need additional theoretical processing to reconstruct the specific piezoelectric tensor elements from the response surface. In addition, samples with non-zero Poisson's ratio would be subject to additional mechanical clamping under the biased PFM tip, which needs to be considered before measured values can be compared with theoretical predictions.⁵⁶

3. CONCLUSIONS

$CuInP_2S_6$ is a very attractive layered ferrielectric featuring a novel quadruple-well potential with four possible non-zero polarization states enabled through the vdW gap and the existence of two polar phases. The theoretical predictions of the stress dependence of strain and polarization have allowed us to derive functions describing mechanical and piezoelectric properties that can be compared with experimental data. The combination of theory and quantitative PFM allows for a direct verification of local polarization states, maps of strain and stress, as well as the c lattice parameter and layer spacing. These results indicate that we enhance the information content

of a single PFM image manifold. The properties can be mapped with lateral resolution of 10s of nm, which allows for insights into material properties on length scales not otherwise easily accessible in a non-destructive way. We verified our findings by comparing with X-ray measurements and discovered that surface domains can relax to a zero-stress state. The procedures we followed open a direct window into the functionality of a complex material and, specifically for CIPS, will enable establishing control over its four polarization states that is crucial to realize new functionalities.

4. METHODS SECTION

4.1. Synthesis. Crystals of heterostructured $CuInP_2S_6/In_{4/3}P_2S_6$ (overall composition $Cu_{0.4}In_{1.2}P_2S_6$) were fabricated using standard vapor transport technique at 775 °C starting with pure (A.A. Puratronic) Cu, S, P, and In_2S_3 , the latter of which was synthesized first to reduce the presence of parasitic phases in the final compound. A detailed description of the CIPS synthesis can be found elsewhere.¹ Measurements were performed on crystals of several μm thickness, and the non-ferroelectric, vacancy-ordered $In_{4/3}P_2S_6$ (IPS) phase which forms through phase separation of the non-stoichiometric sample⁴⁹ was used as the reference point.

4.2. DFT Calculations. The calculations were performed in the same manner as in ref 8, using the ABINIT computer code and norm-conserving pseudopotentials. Here, we summarize the relevant details. The theoretical stress versus strain and polarizations were calculated using the ABINIT v8.2.3 package.⁵⁷ Exchange–correlation effects were treated within the Perdew–Burke–Ernzerhof generalized gradient approximation⁵⁸ with the long-range vdW interaction treated by the DFT-D3 (Becke–Johnson) method.^{59,60} The core–valence electron interactions were modeled by norm-conserving optimized pseudo-potentials⁶¹ generated with OPIUM (<http://opium.sourceforge.net>) and refined via the designed nonlocal methodology.⁶² A 680 eV plane-wave basis-set cutoff energy was used, and the Brillouin zone was sampled using a $4 \times 4 \times 4$ Monkhorst–Pack grid.⁶³ To ensure the numerical accuracy of the stress and polarization values, the energy convergence threshold was $<5 \times 10^{-7}$ eV per unit cell and atomic forces were optimized to be $<5 \times 10^{-4}$ eV \AA^{-1} . The 8-layer surface slab structural relaxation was performed using the Vienna Ab Initio Simulation Package (VASP).⁶⁴ The as-supplied PAW potentials⁶⁵ were used with a 400 eV plane-wave basis-set cutoff energy and the Brillouin zone sampled at the Γ -point. The same treatment of the exchange–correlation and vdW interaction were used. Forces for the slab were optimized to be less than 0.02 eV \AA^{-1} .

4.3. Piezoresponse Force Microscopy. The experiments were performed on a Bruker Icon atomic force microscope in an Ar-filled glovebox. The water and oxygen content in the glove box were below 0.1 ppm. All samples were cleaved inside the protective environment before the measurement. PFM was performed with Pt-coated Budgetsensor ElectriMulti75-G probes (nominal free resonance frequency at 75 kHz; nominal force constant is 3 N/m). PFM was performed using the band excitation technique⁶⁶ which measures the contact resonance peaks that were fitted using a simple harmonic oscillator model to extract PFM amplitude and phase. An image of 256×256 pixels was collected over an area of $3 \times 3 \mu m^2$. The acquisition time was ~ 6 min. The response amplitude was calibrated using standard procedures involving cantilever sensitivity.⁵² After accounting for the instrumental phase offset, the so-called mixed signal was calculated using the product of amplitude and $\cos(\text{phase})$. As the sample has a non-piezoelectric IPS phase, the signal on that phase was used as an offset for electrostatic signal contributions.

■ ASSOCIATED CONTENT

Supporting Information

The Supporting Information is available free of charge at <https://pubs.acs.org/doi/10.1021/acsami.0c09246>.

Discontinuities in the theoretical stress data, procedures to separate CIPS and IPS response, comparison of experimental and theoretical data, and histogram of extracted property maps (PDF)

AUTHOR INFORMATION

Corresponding Author

Nina Balke – Center for Nanophase Materials Sciences, Oak Ridge National Laboratory, Oak Ridge 37831, Tennessee, United States; orcid.org/0000-0001-5865-5892; Email: balken@ornl.gov

Authors

Sabine M. Neumayer – Center for Nanophase Materials Sciences, Oak Ridge National Laboratory, Oak Ridge 37831, Tennessee, United States; orcid.org/0000-0002-8167-1230

John A. Brehm – Department of Physics and Astronomy, Vanderbilt University, Nashville 37235, Tennessee, United States; orcid.org/0000-0001-9176-7845

Lei Tao – Department of Physics and Astronomy, Vanderbilt University, Nashville 37235, Tennessee, United States; Institute of Physics, Chinese Academy of Sciences, Beijing 100190, China

Andrew O'Hara – Department of Physics and Astronomy, Vanderbilt University, Nashville 37235, Tennessee, United States; orcid.org/0000-0002-0323-9039

Panchapakesan Ganesh – Center for Nanophase Materials Sciences, Oak Ridge National Laboratory, Oak Ridge 37831, Tennessee, United States; orcid.org/0000-0002-7170-2902

Stephen Jesse – Center for Nanophase Materials Sciences, Oak Ridge National Laboratory, Oak Ridge 37831, Tennessee, United States

Michael A. Susner – Materials and Manufacturing Directorate, Air Force Research Laboratory, Wright-Patterson Air Force Base, Dayton 45433, Ohio, United States; orcid.org/0000-0002-1211-8749

Michael A. McGuire – Materials Science and Technology Division, Oak Ridge National Laboratory, Oak Ridge 37831, Tennessee, United States; orcid.org/0000-0003-1762-9406

Sokrates T. Pantelides – Department of Physics and Astronomy, Vanderbilt University, Nashville 37235, Tennessee, United States; orcid.org/0000-0002-2963-7545

Petro Maksymovych – Center for Nanophase Materials Sciences, Oak Ridge National Laboratory, Oak Ridge 37831, Tennessee, United States

Complete contact information is available at:

<https://pubs.acs.org/10.1021/acsami.0c09246>

Author Contributions

S.M.N. performed experiments, data analysis, discussion of theoretical and experimental results, and manuscript writing. J.A.B. carried out theoretical calculations. L.T. provided theoretical calculations and contributed to discussion of results. A.O. carried out theoretical calculations, discussion of theoretical and experimental results, and manuscript writing. P.G. supervised and guided theoretical calculations. S.J. provided acquisition software development for experiments. M.A.S. and M.A.M. performed sample synthesis and contributed to manuscript writing. S.T.P. supervised and guided theoretical calculations, contributed to discussion of theoretical and experimental results, and manuscript writing. P.M. and N.B. supervised and guided experiments, discussion of

theoretical and experimental results, and wrote the manuscript. N.B., additionally, carried out data analysis.

Notes

The authors declare no competing financial interest.

ACKNOWLEDGMENTS

The PFM measurements and sample synthesis were supported by the U.S. Department of Energy, Office of Science, Basic Energy Sciences, Materials Science and Engineering Division (S.M.N., P.M., M.A.M., and N.B.). The experiments were conducted at the Center for Nanophase Materials Sciences, which is a DOE Office of Science User Facility which also supported data acquisition software development and support for theoretical calculations (S.J. and P.G.). The theoretical work (J.A.B., L.T., A.O., and S.T.P.), was supported by the U.S. Department of Energy, Office of Science, Division of Materials Science and Engineering under Grant No. DE-FG02-09ER46554 and by the McMinn Endowment at Vanderbilt University. Computations were performed at the National Energy Research Scientific Computing Center, a DOE Office of Science User Facility supported by the Office of Science of the U.S. Department of Energy under contract no. DE-AC02-05CH11231. Manuscript preparation was partially funded by the Air Force Research Laboratory under an Air Force Office of Scientific Research grant (LRIR grant no. 19RXCOR052).

REFERENCES

- (1) Susner, M. A.; Chyasnachyus, M.; McGuire, M. A.; Ganesh, P.; Maksymovych, P. Metal Thio- and Selenophosphates as Multifunctional van der Waals Layered Materials. *Adv. Mater.* **2017**, *29*, 1602852.
- (2) Si, M.; Liao, P.-Y.; Qiu, G.; Duan, Y.; Ye, P. D. Ferroelectric Field-Effect Transistors Based on MoS₂ and CuInP₂S₆ Two-Dimensional van der Waals Heterostructure. *ACS Nano* **2018**, *12*, 6700–6705.
- (3) Neumayer, S. M.; Eliseev, E. A.; Susner, M. A.; Tselev, A.; Rodriguez, B. J.; Brehm, J. A.; Pantelides, S. T.; Panchapakesan, G.; Jesse, S.; Kalinin, S. V.; McGuire, M. A.; Morozovska, A. N.; Maksymovych, P.; Balke, N. Giant Negative Electrostriction and Dielectric Tunability in a van der Waals Layered Ferroelectric. *Phys. Rev. Mater.* **2019**, *3*, 024401.
- (4) Chyasnachyus, M.; Susner, M. A.; Ievlev, A. V.; Eliseev, E. A.; Kalinin, S. V.; Balke, N.; Morozovska, A. N.; McGuire, M. A.; Maksymovych, P. Size-Effect in Layered Ferroelectric CuInP₂S₆. *Appl. Phys. Lett.* **2016**, *109*, 172901.
- (5) Liu, F.; You, L.; Seyler, K. L.; Li, X.; Yu, P.; Lin, J.; Wang, X.; Zhou, J.; Wang, H.; He, H.; Pantelides, S. T.; Zhou, W.; Sharma, P.; Xu, X.; Ajayan, P. M.; Wang, J.; Liu, Z. Room-Temperature Ferroelectricity in CuInP₂S₆ Ultrathin Flakes. *Nat. Commun.* **2016**, *7*, 12357.
- (6) Si, M.; Saha, A. K.; Liao, P.-Y.; Gao, S.; Neumayer, S. M.; Jian, J.; Qin, J.; Balke Wisinger, N.; Wang, H.; Maksymovych, P.; Wu, W.; Gupta, S. K.; Ye, P. D. Room-Temperature Electrocaloric Effect in Layered Ferroelectric CuInP₂S₆ for Solid-State Refrigeration. *ACS Nano* **2019**, *13*, 8760–8765.
- (7) Balke, N.; Neumayer, S. M.; Brehm, J. A.; Susner, M. A.; Rodriguez, B. J.; Jesse, S.; Kalinin, S. V.; Pantelides, S. T.; McGuire, M. A.; Maksymovych, P. Locally Controlled Cu-Ion Transport in Layered Ferroelectric CuInP₂S₆. *ACS Appl. Mater. Interfaces* **2018**, *10*, 27188–27194.
- (8) Brehm, J. A.; Neumayer, S. M.; Tao, L.; O'Hara, A.; Chyasnachyus, M.; Susner, M. A.; McGuire, M. A.; Kalinin, S. V.; Jesse, S.; Ganesh, P.; Pantelides, S. T.; Maksymovych, P.; Balke, N. Tunable quadruple-well ferroelectric van der Waals crystals. *Nat. Mater.* **2020**, *19*, 43–48.

- (9) Jedrecy, N.; Aghavonian, T.; Moussy, J.-B.; Magnan, H.; Stanesco, D.; Portier, X.; Arrio, M.-A.; Mocuta, C.; Vlad, A.; Belkhou, R.; Ohresser, P.; Barbier, A. Cross-Correlation between Strain, Ferroelectricity, and Ferromagnetism in Epitaxial Multiferroic CoFe₂O₄/BaTiO₃ Heterostructures. *ACS Appl. Mater. Interfaces* **2018**, *10*, 28003–28014.
- (10) Gorfman, S.; Simons, H.; Iamsasri, T.; Prasertpalichat, S.; Cann, D. P.; Choe, H.; Pietsch, U.; Watier, Y.; Jones, J. L. Simultaneous Resonant X-Ray Diffraction Measurement of Polarization Inversion and Lattice Strain in Polycrystalline Ferroelectrics. *Sci. Rep.* **2016**, *6*, 20829.
- (11) Schwarzkopf, J.; Braun, D.; Hanke, M.; Uecker, R.; Schmidbauer, M. Strain Engineering of Ferroelectric Domains in KxNa1-xNbO₃ Epitaxial Layers. *Front. Mater.* **2017**, *4* (), DOI: DOI: 10.3389/fmats.2017.00026.
- (12) Catalan, G.; Vlooswijk, A. H. G.; Janssens, A.; Rispens, G.; Redfern, S.; Rijnders, G.; Blank, D. H. A.; Noheda, B. X-Ray Diffraction of Ferroelectric Nanodomains in PbTiO₃ Thin Films. *Integr. Ferroelectr.* **2007**, *92*, 18–29.
- (13) Xu, F.; Trolrier-McKinstry, S.; Ren, W.; Xu, B.; Xie, Z.-L.; Hemker, K. J. Domain Wall Motion and its Contribution to the Dielectric and Piezoelectric Properties of Lead Zirconate Titanate Films. *J. Appl. Phys.* **2001**, *89*, 1336–1348.
- (14) Park, S.-E.; Shrout, T. R. Ultrahigh Strain and Piezoelectric Behavior in Relaxor Based Ferroelectric Single Crystals. *J. Appl. Phys.* **1997**, *82*, 1804–1811.
- (15) Guo, Y.; Liu, Y.; Withers, R. L.; Brink, F.; Chen, H. Large Electric Field-Induced Strain and Antiferroelectric Behavior in (1-x)(Na_{0.5}Bi_{0.5})TiO₃-xBaTiO₃ Ceramics. *Chem. Mater.* **2011**, *23*, 219–228.
- (16) Catalan, G.; Lubk, A.; Vlooswijk, A. H. G.; Snoeck, E.; Magen, C.; Janssens, A.; Rispens, G.; Rijnders, G.; Blank, D. H. A.; Noheda, B. Flexoelectric Rotation of Polarization in Ferroelectric Thin Films. *Nat. Mater.* **2011**, *10*, 963–967.
- (17) Tang, Y. L.; Zhu, Y. L.; Ma, X. L. On the Benefit of Aberration-Corrected HAADF-STEM for Strain Determination and its Application to Tailoring Ferroelectric Domain Patterns. *Ultramicroscopy* **2016**, *160*, 57–63.
- (18) Tang, Y. L.; Zhu, Y. L.; Ma, X. L.; Borisevich, A. Y.; Morozovska, A. N.; Eliseev, E. A.; Wang, W. Y.; Wang, Y. J.; Xu, Y. B.; Zhang, Z. D.; Pennycook, S. J. Observation of a Periodic Array of Flux-Closure Quadrants in Strained Ferroelectric PbTiO₃ Films. *Science* **2015**, *348*, 547.
- (19) Nelson, C. T.; Winchester, B.; Zhang, Y.; Kim, S.-J.; Melville, A.; Adamo, C.; Folkman, C. M.; Baek, S.-H.; Eom, C.-B.; Schlom, D. G.; Chen, L.-Q.; Pan, X. Spontaneous Vortex Nanodomain Arrays at Ferroelectric Heterointerfaces. *Nano Lett.* **2011**, *11*, 828–834.
- (20) Jia, C.-L.; Nagarajan, V.; He, J.-Q.; Houben, L.; Zhao, T.; Ramesh, R.; Urban, K.; Waser, R. Unit-Cell Scale Mapping of Ferroelectricity and Tetragonality in Epitaxial Ultrathin Ferroelectric Films. *Nat. Mater.* **2007**, *6*, 64–69.
- (21) van Helvoort, A. T. J.; Dahl, Ø.; Soleim, B. G.; Holmestad, R.; Tybell, T. Imaging of out-of-plane interfacial strain in epitaxial PbTiO₃/SrTiO₃ thin films. *Appl. Phys. Lett.* **2005**, *86*, 092907.
- (22) Balke, N.; Bdkin, I.; Kalinin, S. V.; Kholkin, A. L. Electromechanical Imaging and Spectroscopy of Ferroelectric and Piezoelectric Materials: State of the Art and Prospects for the Future. *J. Am. Ceram. Soc.* **2009**, *92*, 1629–1647.
- (23) Jesse, S.; Baddorf, A. P.; Kalinin, S. V. Switching Spectroscopy Piezoresponse Force Microscopy of Ferroelectric Materials. *Appl. Phys. Lett.* **2006**, *88*, 062908.
- (24) Jesse, S.; Baddorf, A. P.; Kalinin, S. V. Dynamic Behaviour in Piezoresponse Force Microscopy. *Nanotechnology* **2006**, *17*, 1615–1628.
- (25) Jesse, S.; Vasudevan, R. K.; Collins, L.; Strelcov, E.; Okatan, M. B.; Belianinov, A.; Baddorf, A. P.; Proksch, R.; Kalinin, S. V. Band Excitation in Scanning Probe Microscopy: Recognition and Functional Imaging. *Annu. Rev. Phys. Chem.* **2014**, *65*, 519–536.
- (26) You, L.; Zhang, Y.; Zhou, S.; Chaturvedi, A.; Morris, S. A.; Liu, F.; Chang, L.; Ichinose, D.; Funakubo, H.; Hu, W.; Wu, T.; Liu, Z.; Dong, S.; Wang, J. Origin of Giant Negative Piezoelectricity in a Layered van der Waals Ferroelectric. *Sci. Adv.* **2019**, *5*, No. eaav3780.
- (27) Kocun, M.; Labuda, A.; Gannepalli, A.; Proksch, R. Contact Resonance Atomic Force Microscopy Imaging in Air and Water Using Photothermal Excitation. *Rev. Sci. Instrum.* **2015**, *86*, 083706.
- (28) Rabe, U.; Scherer, V.; Hirsekorn, S.; Arnold, W. Nano-mechanical Surface Characterization by Atomic Force Acoustic Microscopy. *J. Vac. Sci. Technol., B: Microelectron. Nanometer Struct.* **1997**, *15*, 1506–1511.
- (29) Rabe, U.; Amelio, S.; Kopycinska, M.; Hirsekorn, S.; Kempf, M.; Göken, M.; Arnold, W. Imaging and Measurement of Local Mechanical Material Properties by Atomic Force Acoustic Microscopy. *Surf. Interface Anal.* **2002**, *33*, 65–70.
- (30) Stan, G.; King, S. W.; Cook, R. F. Elastic Modulus of Low-k Dielectric Thin Films Measured by Load-Dependent Contact-Resonance Atomic Force Microscopy. *J. Mater. Res.* **2009**, *24*, 2960–2964.
- (31) Wang, W.; Geng, Y.; Wu, W. Background-Free Piezoresponse Force Microscopy for Quantitative Measurements. *Appl. Phys. Lett.* **2014**, *104*, 072905.
- (32) Lei, S.; Koo, T.-Y.; Cao, W.; Eliseev, E. A.; Morozovska, A. N.; Cheong, S.-W.; Gopalan, V. Quantitative Lateral and Vertical Piezoresponse Force Microscopy on a PbTiO₃ Single Crystal. *J. Appl. Phys.* **2016**, *120*, 124106.
- (33) Soergel, E. Piezoresponse Force Microscopy (PFM). *J. Phys. D: Appl. Phys.* **2011**, *44*, 464003.
- (34) Pan, K.; Liu, Y. M.; Peng, J. L.; Liu, Y. Y. Double-Tip Piezoresponse Force Microscopy for Quantitative Measurement of the Piezoelectric Coefficient at the Nanoscale. *Europhys. Lett.* **2013**, *104*, 67001.
- (35) Dharmasena, S. M.; Yang, Z.; Kim, S.; Bergman, L. A.; Vakakis, A. F.; Cho, H. Ultimate Decoupling between Surface Topography and Material Functionality in Atomic Force Microscopy Using an Inner-Padded Cantilever. *ACS Nano* **2018**, *12*, 5559–5569.
- (36) Lepadatu, S.; Stewart, M.; Cain, M. G. Quantification of Electromechanical Coupling Measured With Piezoresponse Force Microscopy. *J. Appl. Phys.* **2014**, *116*, 066806.
- (37) Shetty, S.; Yang, J. I.; Stitt, J.; Trolrier-McKinstry, S. Quantitative and High Spatial Resolution d33 Measurement of Piezoelectric Bulk and Thin Films. *J. Appl. Phys.* **2015**, *118*, 174104.
- (38) Labuda, A.; Proksch, R. Quantitative Measurements of Electromechanical Response With a Combined Optical Beam and Interferometric Atomic Force Microscope. *Appl. Phys. Lett.* **2015**, *106*, 253103.
- (39) Balke, N.; Jesse, S.; Yu, P.; Ben Carmichael, B.; Kalinin, S. V.; Tselev, A. Quantification of Surface Displacements and Electro-mechanical Phenomena via Dynamic Atomic Force Microscopy. *Nanotechnology* **2016**, *27* (), DOI: DOI: 10.1088/0957-4484/27/42/425707.
- (40) Bradler, S.; Schirmeisen, A.; Roling, B. Amplitude Quantification in Contact-Resonance-Based Voltage-Modulated Force Spectroscopy. *J. Appl. Phys.* **2017**, *122*, 065106.
- (41) Kalinin, S. V.; Bonnell, D. A. Contrast Mechanism Maps for Piezoresponse Force Microscopy. *J. Mater. Res.* **2002**, *17*, 936–939.
- (42) He, L.; Meng, J.; Zhao, B.; Jiang, J.; Geng, W.; Jiang, A. Buckling Effect Induced Abnormal Out of Plane Domain Stripe in BiFeO₃ Single-Crystalline Thin Film Investigated by Piezoresponse Force Microscopy. *Ferroelectrics* **2016**, *492*, 59–68.
- (43) Jesse, S.; Guo, S.; Kumar, A.; Rodriguez, B. J.; Proksch, R.; Kalinin, S. V. Resolution Theory, and Static and Frequency-Dependent Cross-Talk in Piezoresponse Force Microscopy. *Nanotechnology* **2010**, *21*, 405703.
- (44) Balke, N.; Jesse, S.; Carmichael, B.; Okatan, M. B.; Kravchenko, I. I.; Kalinin, S. V.; Tselev, A. Quantification of In-Contact Probe-Sample Electrostatic Forces with Dynamic Atomic Force Microscopy. *Nanotechnology* **2017**, *28*, 065704.

- (45) Kim, Y.; Kumar, A.; Tselev, A.; Kravchenko, I. I.; Han, H.; Vrejoiu, I.; Lee, W.; Hesse, D.; Alexe, M.; Kalinin, S. V.; Jesse, S. Nonlinear Phenomena in Multiferroic Nanocapacitors: Joule Heating and Electromechanical Effects. *ACS Nano* **2011**, *5*, 9104–9112.
- (46) Balke, N.; Jesse, S.; Li, Q.; Maksymovych, P.; Baris Okatan, M.; Strelcov, E.; Tselev, A.; Kalinin, S. V. Current and Surface Charge Modified Hysteresis Loops in Ferroelectric Thin Films. *J. Appl. Phys.* **2015**, *118*, 072013.
- (47) Balke, N.; Maksymovych, P.; Jesse, S.; Kravchenko, I. I.; Li, Q.; Kalinin, S. V. Exploring Local Electrostatic Effects with Scanning Probe Microscopy: Implications for Piezoresponse Force Microscopy and Triboelectricity. *ACS Nano* **2014**, *8*, 10229–10236.
- (48) Balke, N.; Kalnaus, S.; Dudney, N. J.; Daniel, C.; Jesse, S.; Kalinin, S. V. Local Detection of Activation Energy for Ionic Transport in Lithium Cobalt Oxide. *Nano Lett.* **2012**, *12*, 3399–3403.
- (49) Susner, M. A.; Belianinov, A.; Borisevich, A.; He, Q.; Chyashnavichyus, M.; Demir, H.; Sholl, D. S.; Ganesh, P.; Abernathy, D. L.; McGuire, M. A.; Maksymovych, P. High-Tc Layered Ferroelectric Crystals by Coherent Spinodal Decomposition. *ACS Nano* **2015**, *9*, 12365–12373.
- (50) Maisonneuve, V.; Evain, M.; Payen, C.; Cajipe, V. B.; Molinié, P. Room-temperature crystal structure of the layered phase CuInIIIP2S6. *J. Alloys Compd.* **1995**, *218*, 157–164.
- (51) Vasudevan, R. K.; Balke, N.; Maksymovych, P.; Jesse, S.; Kalinin, S. V. Ferroelectric or Non-Ferroelectric: Why So Many Materials Exhibit “Ferroelectricity” on the Nanoscale. *Appl. Phys. Rev.* **2017**, *4*, 021302.
- (52) Balke, N.; Jesse, S.; Yu, P.; Ben Carmichael, C.; Kalinin, S. V.; Tselev, A. Quantification of Surface Displacements and Electro-mechanical Phenomena via Dynamic Atomic Force Microscopy. *Nanotechnology* **2016**, *27*, 425707.
- (53) de Jong, M.; Chen, W.; Geerlings, H.; Asta, M.; Persson, K. A. A Database to Enable Discovery and Design of Piezoelectric Materials. *Sci. Data* **2015**, *2*, 150053.
- (54) Jin, Y.; Lu, X.; Zhang, J.; Kan, Y.; Bo, H.; Huang, F.; Xu, T.; Du, Y.; Xiao, S.; Zhu, J. Studying the Polarization Switching in Polycrystalline BiFeO3 Films by 2D Piezoresponse Force Microscopy. *Sci. Rep.* **2015**, *5*, 12237.
- (55) Kalinin, S. V.; Rodriguez, B. J.; Jesse, S.; Karapetian, E.; Mirman, B.; Eliseev, E. A.; Morozovska, A. N. Nanoscale Electromechanics of Ferroelectric and Biological Systems: A New Dimension in Scanning Probe Microscopy. *Annu. Rev. Mater. Res.* **2007**, *37*, 189–238.
- (56) Eliseev, E. A.; Kalinin, S. V.; Jesse, S.; Bravina, S. L.; Morozovska, A. N. Electromechanical Detection in Scanning Probe Microscopy: Tip Models and Materials Contrast. *J. Appl. Phys.* **2007**, *102*, 014109.
- (57) Gonze, X.; Beuken, J.-M.; Caracas, R.; Detraux, F.; Fuchs, M.; Rignanese, G.-M.; Sindic, L.; Verstraete, M.; Zerah, G.; Jollet, F.; Torrent, M.; Roy, A.; Mikami, M.; Ghosez, P.; Raty, J.-Y.; Allan, D. C. First-Principles Computation of Material Properties: the ABINIT Software Project. *Comput. Mater. Sci.* **2002**, *25*, 478–492.
- (58) Perdew, J. P.; Burke, K.; Ernzerhof, M. Generalized Gradient Approximation Made Simple. *Phys. Rev. Lett.* **1996**, *77*, 3865.
- (59) Grimme, S.; Antony, J.; Ehrlich, S.; Krieg, H. A Consistent and Accurate Ab Initio Parametrization of Density Functional Dispersion Correction (DFT-D) for the 94 Elements H-Pu. *J. Chem. Phys.* **2010**, *132*, 154104.
- (60) Grimme, S.; Ehrlich, S.; Goerigk, L. Effect of the Damping Function in Dispersion Corrected Density Functional Theory. *J. Comput. Chem.* **2011**, *32*, 1456–1465.
- (61) Rappe, A. M.; Rabe, K. M.; Kaxiras, E.; Joannopoulos, J. D. Optimized Pseudopotentials. *Phys. Rev. B: Condens. Matter Mater. Phys.* **1990**, *41*, 1227–1230.
- (62) Ramer, N. J.; Rappe, A. M. Designed Nonlocal Pseudopotentials for Enhanced Transferability. *Phys. Rev. B: Condens. Matter Mater. Phys.* **1999**, *59*, 12471–12478.
- (63) Monkhorst, H. J.; Pack, J. D. Special Points For Brillouin-Zone Integrations. *Phys. Rev. B: Condens. Matter Mater. Phys.* **1976**, *13*, 5188–5192.
- (64) Kresse, G.; Furthmüller, J. Efficient iterative schemes for ab initio total-energy calculations using a plane-wave basis set. *Phys. Rev. B: Condens. Matter Mater. Phys.* **1996**, *54*, 11169–11186.
- (65) Kresse, G.; Joubert, D. From Ultrasoft Pseudopotentials to the Projector Augmented-Wave Method. *Phys. Rev. B: Condens. Matter Mater. Phys.* **1999**, *59*, 1758–1775.
- (66) Jesse, S.; Kalinin, S. V.; Proksch, R.; Baddorf, A. P.; Rodriguez, B. J. The Band Excitation Method in Scanning Probe Microscopy for Rapid Mapping of Energy Dissipation on the Nanoscale. *Nanotechnology* **2007**, *18*, 435503.